LUND UNIVERSITY

A numerical comparison of 2D resistivity imaging with 10 electrode arrays

Dahlin, Torleif; Zhou, Bing

Published in:
Geophysical Prospecting

DOI:
10.1111/j.1365-2478.2004.00423.x

2004

Link to publication

Citation for published version (APA):
Dahlin, T., & Zhou, B. (2004). A numerical comparison of 2D resistivity imaging with 10 electrode arrays. *Geophysical Prospecting*, *52*(5), 379-398. https://doi.org/10.1111/j.1365-2478.2004.00423.x

Total number of authors:
2

General rights
Unless other specific re-use rights are stated the following general rights apply:
Copyright and moral rights for the publications made accessible in the public portal are retained by the authors and/or other copyright owners and it is a condition of accessing publications that users recognise and abide by the legal requirements associated with these rights.
• Users may download and print one copy of any publication from the public portal for the purpose of private study or research.
• You may not further distribute the material or use it for any profit-making activity or commercial gain
• You may freely distribute the URL identifying the publication in the public portal

Read more about Creative commons licenses: https://creativecommons.org/licenses/

Take down policy
If you believe that this document breaches copyright please contact us providing details, and we will remove access to the work immediately and investigate your claim.

LUND UNIVERSITY

PO Box 117
221 00 Lund
+46 46-222 00 00

Geophysical Prospecting, 2004, **52**, 379–398

A numerical comparison of 2D resistivity imaging with 10 electrode arrays

Torleif Dahlin[1]* and Bing Zhou[2]

[1]*Department of Engineering Geology, Lund University, PO Box 118, 221 00 Lund, Sweden, and* [2]*Department of Geology and Geophysics, School of Earth and Environmental Sciences, Adelaide University, SA 5005 Adelaide, Australia*

Received January 2002, revision accepted April 2004

ABSTRACT

Numerical simulations are used to compare the resolution and efficiency of 2D resistivity imaging surveys for 10 electrode arrays. The arrays analysed include pole-pole (PP), pole-dipole (PD), half-Wenner (HW), Wenner-α (WN), Schlumberger (SC), dipole-dipole (DD), Wenner-β (WB), γ-array (GM), multiple or moving gradient array (GD) and midpoint-potential-referred measurement (MPR) arrays. Five synthetic geological models, simulating a buried channel, a narrow conductive dike, a narrow resistive dike, dipping blocks and covered waste ponds, were used to examine the surveying efficiency (anomaly effects, signal-to-noise ratios) and the imaging capabilities of these arrays. The responses to variations in the data density and noise sensitivities of these electrode configurations were also investigated using robust (L_1-norm) inversion and smoothness-constrained least-squares (L_2-norm) inversion for the five synthetic models.

The results show the following. (i) GM and WN are less contaminated by noise than the other electrode arrays. (ii) The relative anomaly effects for the different arrays vary with the geological models. However, the relatively high anomaly effects of PP, GM and WB surveys do not always give a high-resolution image. PD, DD and GD can yield better resolution images than GM, PP, WN and WB, although they are more susceptible to noise contamination. SC is also a strong candidate but is expected to give more edge effects. (iii) The imaging quality of these arrays is relatively robust with respect to reductions in the data density of a multi-electrode layout within the tested ranges. (iv) The robust inversion generally gives better imaging results than the L_2-norm inversion, especially with noisy data, except for the dipping block structure presented here. (v) GD and MPR are well suited to multichannel surveying and GD may produce images that are comparable to those obtained with DD and PD. Accordingly, the GD, PD, DD and SC arrays are strongly recommended for 2D resistivity imaging, where the final choice will be determined by the expected geology, the purpose of the survey and logistical considerations.

INTRODUCTION

DC electrical resistivity surveying is a popular geophysical exploration technique because of its simple physical principle and efficient data acquisition. Traditional resistivity measurements are carried out on the earth's surface with a specified array in order to obtain apparent-resistivity sounding curves, apparent-resistivity profiling data or apparent-resistivity pseudosections, all of which qualitatively reflect the vertical or horizontal variations in subsurface resistivity. This technique is widely used in groundwater, civil engineering and

*E-mail: Torleif.Dahlin@tg.lth.se

© 2004 European Association of Geoscientists & Engineers

environmental investigations. In the last decade, there have been great improvements in computerized data acquisition systems and 2D and 3D inversion software, so that resistivity imaging or resistivity tomography has become an increasingly attractive exploration technique. Many geophysicists have shown that it is possible to reconstruct an accurate resistivity image of the subsurface using a large number of measured data (with enough spatial samples and coverage) and employing 2D or 3D imaging or inversion schemes (Daily and Owen 1991; Park and Van 1991; Shima 1992; Li and Oldenburg 1992; Sasaki 1994; Loke and Barker 1995, 1996; LaBrecque *et al*. 1996).

Since the 1950s, many different electrode arrays have been used in electrical exploration techniques, such as pole-pole (PP), pole-dipole (PD), half-Wenner (HW), Wenner-α (WN), Wenner-Schlumberger (SC), dipole-dipole (DD), Wenner-β (WB) and γ-array (GM) (see Fig. 1). HW is a special case of PD with the factor n equal to one. Similarly WB is a special case of DD and WN is a special case of SC. In addition, the two electrode configurations that we call the multiple or moving gradient array (GD) and the midpoint-potential-referred measurements (MPR) (see Fig. 1) are very suitable for a multichannel-recording system. The arrays enable many simultaneous measurements to be made for each current injection point, thus reducing the fieldwork time significantly. Each of the 10 electrode configurations has its own advantages and limitations in fieldwork. They provide useful practical options for surface sounding, profiling and scanning surveys in different situations. Some of them are now frequently employed in 2D or 3D resistivity imaging applications, namely PP, WN, SC, PD and DD (Dahlin 1996; Chambers *et al*. 1999; Storz, Storz and Jacobs 2000). In principle, the PP data set is the most elementary data set, because the data from other arrays may be obtained by linear combinations of the PP data. Unfortunately, it is often difficult to acquire pure PP data in the field due to limited access for the remote electrodes (Park and Van 1991; Van, Park and Hamilton 1991), and furthermore a long potential reference electrode layout is prone to picking up noise.

For resistivity imaging, or tomography, there might be differences in the imaging abilities of the 10 electrode arrays when applied to a geological model, i.e. differences in spatial resolution, in tendency to produce artefacts in the images, in deviation from the true model resistivity and in interpretable maximum depth. The sensitivity patterns (see the backgrounds of the diagrams in Fig. 1) play an important role in the resolving capability of an array in the inversion of the data. A considerable amount of research has been devoted to examining the relative merits of using some of the arrays for resistivity imaging; for example, Sasaki (1992) synthetically compared the resolution of cross-hole resistivity tomography using PP, PD and DD arrays. He suggested that DD surveying, when the instrument accuracy is high, is more suitable for resolving complex structures than the PP array, and that PD may present a good compromise between resolution and signal strength. Recently, Oldenburg and Li (1999), analysing the 'depth of investigation', reaffirmed the different depths of penetration achieved by PP, PD and DD arrays in the inverted models.

Dahlin and Loke (1998) and Olayinka and Yaramanci (2000), respectively, examined the imaging resolution and reliability of a WN array. They pointed out that the WN data density is important for the resolution capability and that the inverted model provides only an approximate guide to the true geometry and true formation resistivity. Zhou and Greenhalgh (2000) studied some specific electrode configurations for cross-hole resistivity imaging. Obviously, a comprehensive comparison of the imaging abilities of these electrode arrays is required in order to assess the suitability of their behaviour for practical imaging applications. More research is needed into the use of these arrays for imaging in order to assess their characteristics more fully. In this way, it will be possible to predict which features of the earth model can be resolved and which details cannot be resolved in imaging surveys using these different electrode arrays. In addition, for fieldwork design and data interpretation, the spatial resolutions and the noise sensitivities of the arrays should be known.

In order to obtain a reliable high-resolution image, the electrode array used should ideally give data with the maximum anomaly information, reasonable data coverage and a high signal-to-noise ratio. In imaging data acquisition, a multi-electrode cable with a fixed inter-electrode spacing is often employed. Different data acquisition schemes with different electrode arrays (controlled by the array parameters a and n, see Fig. 1) can be measured with such a system. Theoretically, a complete data set of an array (using a and n consecutively) with low noise contamination is needed in order to obtain a high-resolution image, but acquiring a large number of data points significantly increases the fieldwork time even when using an automatic data acquisition system. On the other hand, a large number of data points can also increase the difficulty in reaching a good data misfit from an inversion and will probably produce more artefacts due to the unknown characteristics of the noise contamination (LaBrecque *et al*. 1996; Zhou and Dahlin 2003).

To apply these electrode configurations effectively and efficiently, it is necessary to devise efficient measurement schemes for the arrays. The following questions need to be answered: (i) How does the resolution of these configurations change with the array parameters (a and n) in a multi-electrode layout? (ii) What are the most efficient survey patterns for these arrays needed to obtain the basic features of the subsurface? To our knowledge, a detailed study of efficient surveying methods using the 10 electrode arrays has not yet been carried out for 2D imaging. Such a study can be very helpful in the design of fieldwork methodology and the interpretation of field data for practical applications.

We investigate numerically the behaviour of the 10 electrode arrays when used to image five synthetic models, which reflect some geological structures in practice. Two popular inversion schemes – robust inversion and smoothness-constrained least-squares inversion – were applied in this work and a comprehensive comparison of all the electrode arrays for 2D resistivity imaging was made. The following aspects were compared: the resolution obtained for the different geological models, the imaging quality obtained with different data densities and the sensitivity to noise levels.

This paper is organized into four sections. In the first section, we briefly describe and illustrate 2D imaging measurement schemes for the different electrode arrays. In the second section, the five synthetic models used in the imaging experiments are described. In the third section, we show some specific imaging results obtained using different inversion schemes, different data densities and different noise levels, which demonstrate the behaviour of the electrode arrays in different resistivity imaging applications. In the fourth section, we summarize the advantages and disadvantages of the different electrode arrays for imaging surveys in terms of the numerical experiments. This summary may be a general guide to the application of the 2D imaging technique.

2D RESISTIVITY IMAGING SURVEY

Figure 1 shows schematically the 10 electrode arrays considered in this work. Their sensitivity patterns are also given in the diagrams. From this figure, it can be seen that, except for PP, HW, WN and WB, the configurations have many combinations of the parameters a and n, which can be adapted depending on the required spatial resolution, penetration depth and background noise at a field site. In general, a larger spacing a and larger n give relatively deeper information about the earth's structure, while a small spacing a or small n may offer a relatively good horizontal resolution for the shallower sections of the ground. Normally, 2D resistivity imaging surveying is carried out to obtain a good coverage of data along an observation line with one of these configurations. This can be carried out with an 81-electrode layout, for example, as with the Lund Imaging System (Dahlin 1993).

Table 1 gives three examples of survey designs with different data densities (namely Survey 1, Survey 2 and Survey 3) for PP, PD, HW, DD, GM, GD and MPR imaging surveys. We assume that the basic spacing is 1 m and the maximum separation of the electrodes is 60 m for all the electrode configurations. This assumption does not affect the generality because the basic spacing can be changed arbitrarily, thus changing the maximum separation correspondingly, but the imaging survey controlled by a and n will still be similar to those shown in Table 1. With this assumption, WN and WB have a maximum of 990 data points, SC has 1710 data points over the range of $a = 1{\sim}5$ m and $n = 1{\sim}7$, while the other seven arrays may have quite different numbers of data points for the various surveys. From Table 1, it can be seen that there is a factor of about two in the number of data points between any two of the three surveys. This means that the survey time for Survey 2 or Survey 1 would be two or four times longer using a single-channel instrument. In order to investigate effective and efficient survey methods with these arrays, we list only one survey type for WN and WB arrays (the complete data sets), and two surveys for the SC array by assigning different values to a and n (see Table 1) under the assumption that the data points in each survey are comparable. To view the data densities of the different surveys, Fig. 2 shows the data point distribution in the ρ_a-pseudosections of Survey 3 as an example.

From the surveying point of view, it is well known that the spatial resolution and the penetration depth of an electrode array are related to the basic spacing and the maximum separation of electrodes. Thus, the three surveying schemes shown in Table 1 give approximate resolution limits and similar penetration depths for all the electrode arrays, because the same basic spacing and the maximum separation of electrodes are used. However, the exact resolution and penetration depth of the arrays also depend on the geological models (electrical properties, anomaly body geometry) and the noise contamination levels, all of which may be efficiently simulated by numerical methods, thus demonstrating the capabilities of imaging surveys using the parameters in Table 1.

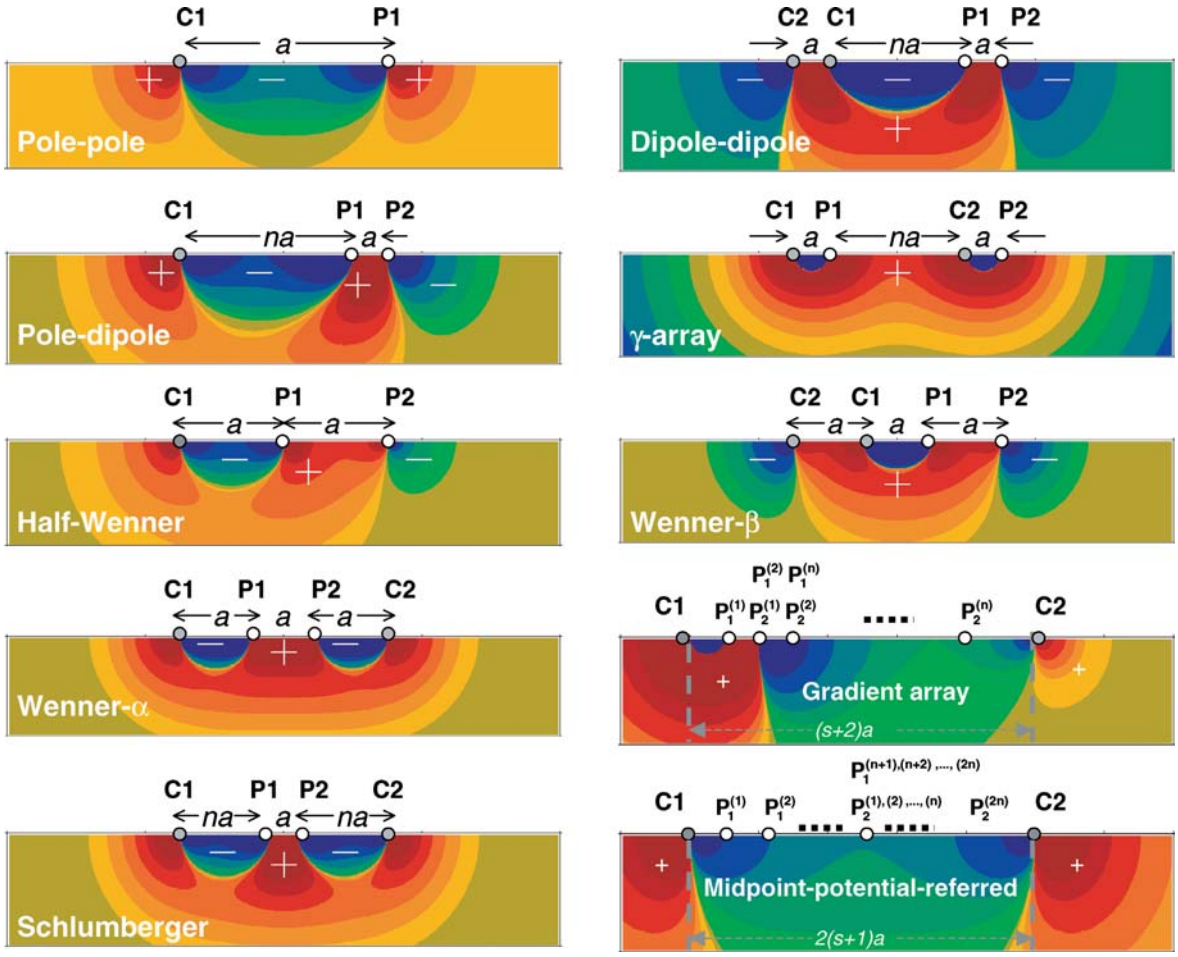

Figure 1 Schematic diagrams of electrode arrays and their sensitivity patterns for 2D resistivity surveys. C1 and C2 are positive and negative current electrodes, respectively. P1 and P2 are two potential electrodes. The italic letters *a*, *n* and *s* are the array parameters that control the spacing and maximum separation of the arrays in a multi-electrode layout. The sensitivity patterns for the gradient and midpoint-potential-referred arrays are just one example of each of the indicated potential electrode combinations.

SYNTHETIC GEOLOGICAL MODELS

To investigate the imaging capabilities of these electrode configurations, we designed four different model geometries (see Fig. 3), which represent various geological or environmental situations. The first model simulates a buried channel of coarse-grained sediments (Fig. 3a), which consists of a 2.5 m-thick upper layer of resistivity 70 Ωm that decreases in thickness towards the right end of the model. This layer rests on a bottom layer of resistivity 30 Ωm and has an embedded trapezoidal structure of resistivity 200 Ωm reaching to a maximum depth of 11 m. Geologically, this could be a simplified model of an old river channel in a clay environment, which has been covered by silty sediments. The second model is a narrow dike model with overburden (Fig. 3b). It consists of a 2 m-wide dike of low/high resistivity (50/300 Ωm) in a host rock of high/low resistivity (1000/50 Ωm), and the dike structure is covered by a 2.5 m-thick layer of resistivity 200 Ωm. This situation could be a fractured or weathered zone in crystalline rock, or a resistive intrusive dike in sedimentary rock, under a cover of sediments or till. The third model (Fig. 3c) is composed of a sequence of dipping blocks of different widths under a top layer of resistivity 200 Ωm. The resistivities of the blocks are alternately 100 Ωm and 300 Ωm. This model simulates a tilted sequence of sedimentary rocks under a layer of till or coarse-grained sediments. The last model (Fig. 3d) was inspired by a field survey over a waste pond in southern Sweden (Bernstone and Dahlin 1996), where a number of pits

Table 1 Examples of surveying schemes for 2D resistivity imaging (based on an 81-electrode layout with 1 m spacing)

Configuration	Survey 1	Survey 2	Survey 3
Pole-pole (PP)	$a = 1{\sim}60$ m, scanning for each electrode; data points: 3030	$a = 1{\sim}60$ m, scanning for every two electrodes; data points: 1530	$a = 1, 3, 5, \ldots, 59$ m, scanning for every two electrodes; data points: 765
Pole-dipole (PD)	$a = 1, 3, 5, 8$ m, $n = 1{\sim}6$, forward and reverse scanning for each electrode; data points: 2970	$a = 1, 3, 5, 8$ m, $n = 1{\sim}6$, forward and reverse scanning for every two electrodes; data points: 1500	$a = 1$ m, $n = 1, 2, 3$; $a = 3$ m, $n = 2, 3, 4$; $a = 5$ m, $n = 3, 4, 5$; $a = 8$ m, $n = 4, 5, 6$; forward and reverse scanning for every two electrodes; data points: 715
Half-Wenner (HW)	$a = 1{\sim}30$ m, scanning for each electrode; data points: 3000	$a = 1{\sim}30$ m, scanning for every two electrodes; data points: 1530	$a = 1, 3, \ldots, 29$ m, scanning for every two electrodes; data points: 778
Wenner-α (WN)			$a = 1{\sim}20$ m, scanning for each electrode; data points: 990
Schlumberger (SC)		$a = 1{\sim}5$ m, $n = 1{\sim}6$; scanning for each electrode; data points: 1710	$a = 1$ m, $n = 1, 2, 3$; $a = 2$ m, $n = 2, 3, 4$; $a = 3$ m, $n = 3, 4, 5$; $a = 4$ m, $n = 4, 5, 6$; scanning for each electrode; data points: 780
Dipole-dipole (DD)	$a = 1{\sim}7$ m, $n = 1{\sim}6$; scanning for each electrode; data points: 2478	$a = 1{\sim}7$ m, $n = 1{\sim}6$; scanning for every two electrodes; data points: 1254	$a = 1{\sim}7$ m, $n = 1, 3, 4, 6$; scanning for every two electrodes; data points: 836
Wenner-β (WB)			$a = 1{\sim}20$ m, scanning for each electrode; data points: 990
γ-array (GM)	$a = 1{\sim}7$ m, $n = 1{\sim}6$; scanning for each electrode; data points: 2478	$a = 1{\sim}7$ m, $n = 1{\sim}6$; scanning for every two electrodes; data points: 1254	$a = 1{\sim}7$ m, $n = 1, 3, 4, 6$; scanning for every two electrodes; data points: 836
Multiple gradient array (GD)	$a = 1$, $s = 15, 30, 58$; scanning for each electrode; data points: 3648	$a = 1$, $s = 15, 30, 58$; scanning for every two electrodes; data points: 1861	$a = 1, 2$, $s = 13$; $a = 3$, $s = 18$; scanning for every two electrodes; data points: 965
Midpoint-potential-referred measurement (MPR)	$a = 1$, $s = 9, 19, 29$; scanning for each electrode; data points: 3874	$a = 1$, $s = 9, 19, 29$; scanning for every two electrodes; data points: 1994	$a = 1$, $s = 6$; $a = 2$, $s = 6$; $a = 3$, $s = 9$; scanning for every two electrodes; data points: 930

were excavated in limestone (resistivity 100 Ωm) quarry waste fill material. The pits were used for disposing of various waste sludges, which were characterized by low resistivity (10 Ωm), different thicknesses and various depths. We used the four models as representatives of geological structures, and hoped that the synthetic imaging for the four models would indicate the imaging abilities of the 10 arrays.

MEASUREMENT EFFECTIVENESS

The anomaly effect, developed by Militer, Rosler and Losch (1979), is commonly used to evaluate the effectiveness of resistivity measurements of an electrode array. From the imaging point of view, for an effective survey, the value of the anomaly effect should be significantly greater than the background noise. Firstly, we examined the anomaly effects of the electrode arrays on the four synthetic models. Using our 2.5D resistivity modelling software (Zhou and Greenhalgh 2000), we calculated the mean values of the absolute anomaly effects using the potentials generated with and without the geological targets (buried channel, narrow dike, dipping blocks and waste ponds). Before the calculations, the numerical modelling accuracy was examined using a cell-size of 0.5 m and 40 wavenumbers so as to achieve a computational error

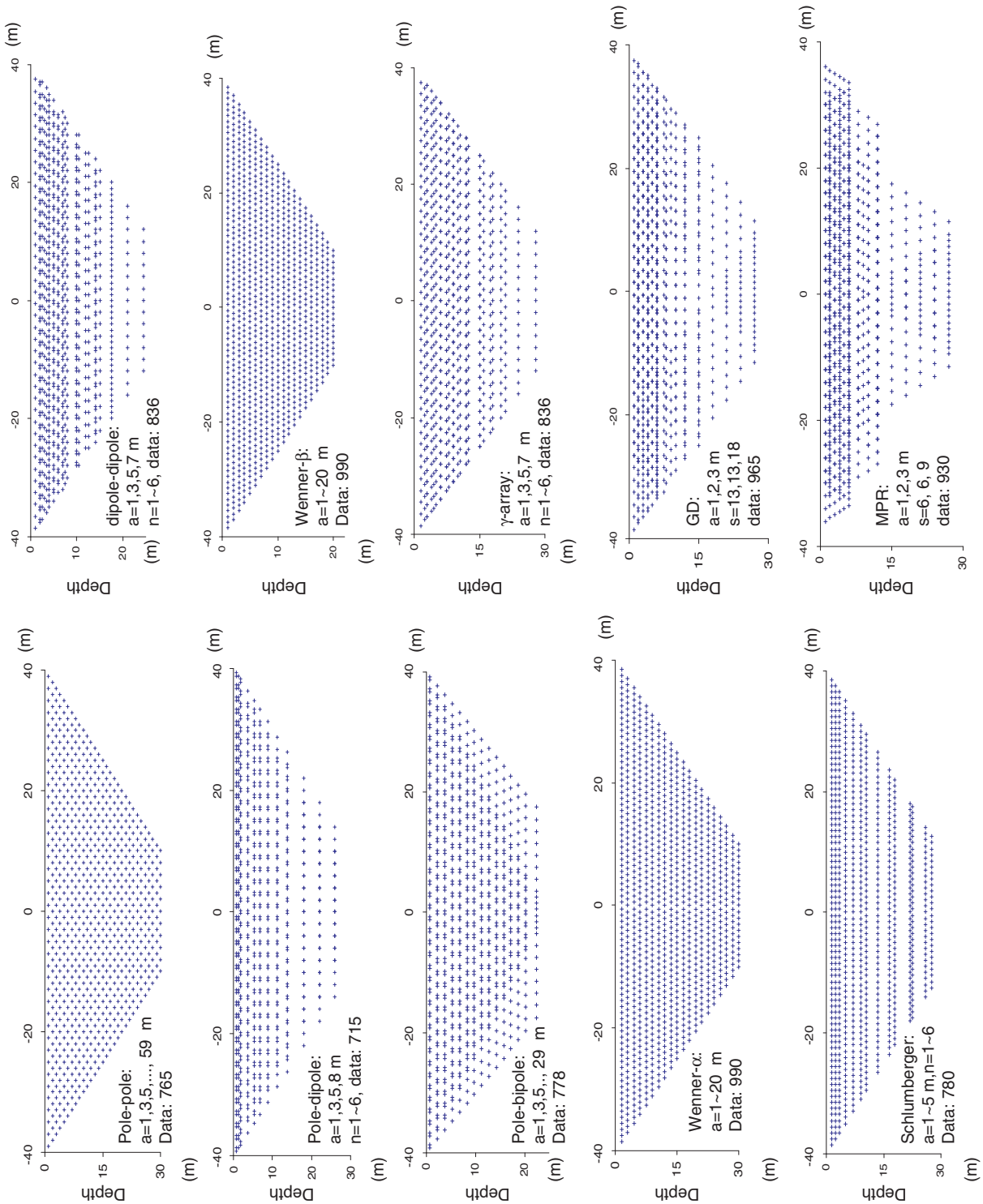

Figure 2 Distribution of data points of Survey 3 in Table 1 for the 10 electrode arrays shown in Fig. 1.

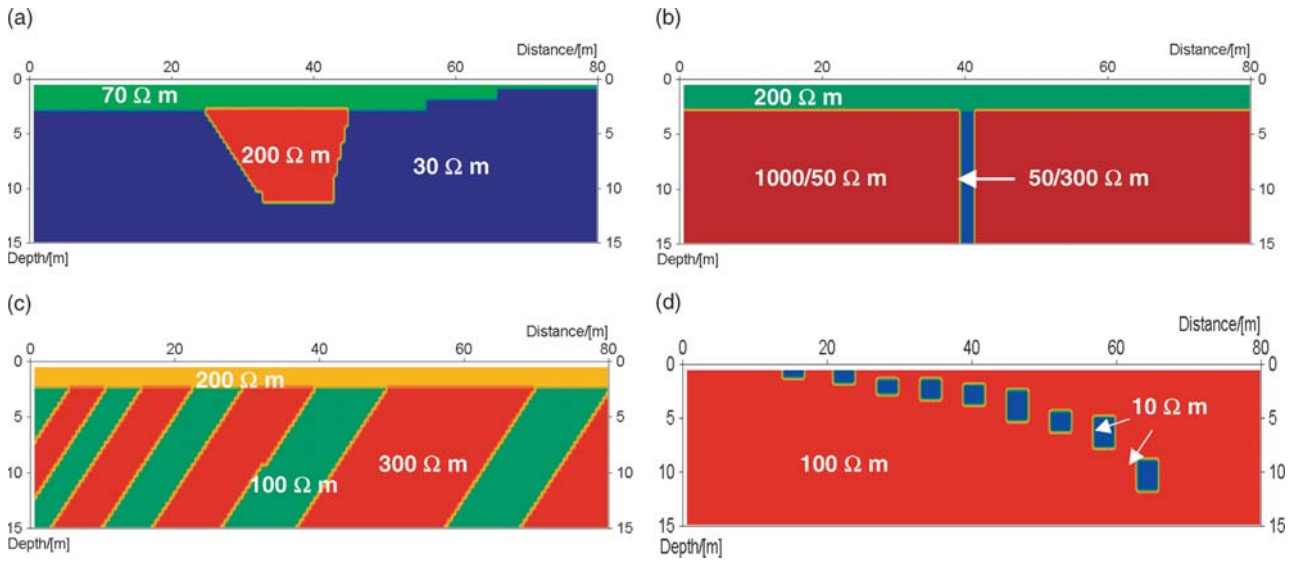

Figure 3 Synthetic models for numerical imaging experiments. (a) A simplified model of an old river channel in a clay environment covered by silty sediments. (b) A dike model that represents a fractured or weathered zone in crystalline rock under a cover of coarse-grained sediment; a model with the same geometry but a highly resistive dike was also used. (c) Dipping blocks of different widths, intended to simulate sedimentary rocks under a layer of till. (d) A waste pond model simulating a field site in southern Sweden.

of less than 2%. Figure 4 shows the results for all 10 electrode arrays and the three surveying schemes. From these diagrams, it can be seen that the anomaly effects of the arrays vary with the geological model; for example, PP gives the smallest values of the anomaly effect on the buried channel and waste pond structures (Figs 4a,d), but on the conductive dike and dipping block models it gives the largest values among the arrays (Figs 4b,c). On the resistive dike model, GM presents much lower anomaly effects than other arrays (Fig. 4b), but on the other models it is comparable. It can also be seen that, for the three surveying schemes in Table 1, there are no significant changes in the anomaly effects for the five geological models.

In practical applications, the observed data are usually contaminated by different kinds of noise. In recent years, we have carried out an investigation into the properties and the effects of the observation noise using several field data sets, which were obtained by analyses of normal and reciprocal measurements at each data point. Using statistical analysis, we found that the observed potential errors at different sites demonstrated a general trend – an increase by a power with decreasing potential value (Zhou and Dahlin 2003), i.e. $\beta = (c_1/U)^{c_2}$, where β denotes the absolute relative error (%) of the potential observations, U denotes the potential reading, and c_1 and c_2 are positive constants that may vary with field sites and measurement times. This function gives the main feature of the background noise except for larger outliers due to various incidents during fieldwork. It implies that the noise contamination of data generally depends on the observed potential of an electrode array (potential-dependent). We used the error property to simulate observation noise, which is generated by the formula: *noisy data* $= U(1 + R)\beta/100$, where R is a random number. By assigning different values to c_1 and c_2, we simulated different noise levels.

Figure 5 shows an example of the synthetic noise which was applied to the conductive dike model (Fig. 3b) using the Survey 1 parameters (Table 1). It can be seen that the noise contamination of the survey data may differ for different electrode arrays due to the differences in the potential responses to the dike model. From this simulation, we obtain the sequence: GM, WN, PP, SC, MPR, HW, WB, PD, GD and DD, in terms of the increase in contamination (mean value ε or standard variation σ). Similar results were obtained with the other three geological models in Fig. 3. This implies that GM and WN surveys are less prone to be contaminated by random noise than the other arrays in imaging surveys, and that DD, GD, PD and WB surveys have a larger risk of noise contamination than the other configurations. The synthetic noise is very similar to field observations at various sites (Zhou and Dahlin 2003). Figure 6 shows the pseudosections of the noise-contaminated apparent resistivity of the conductive dike model.

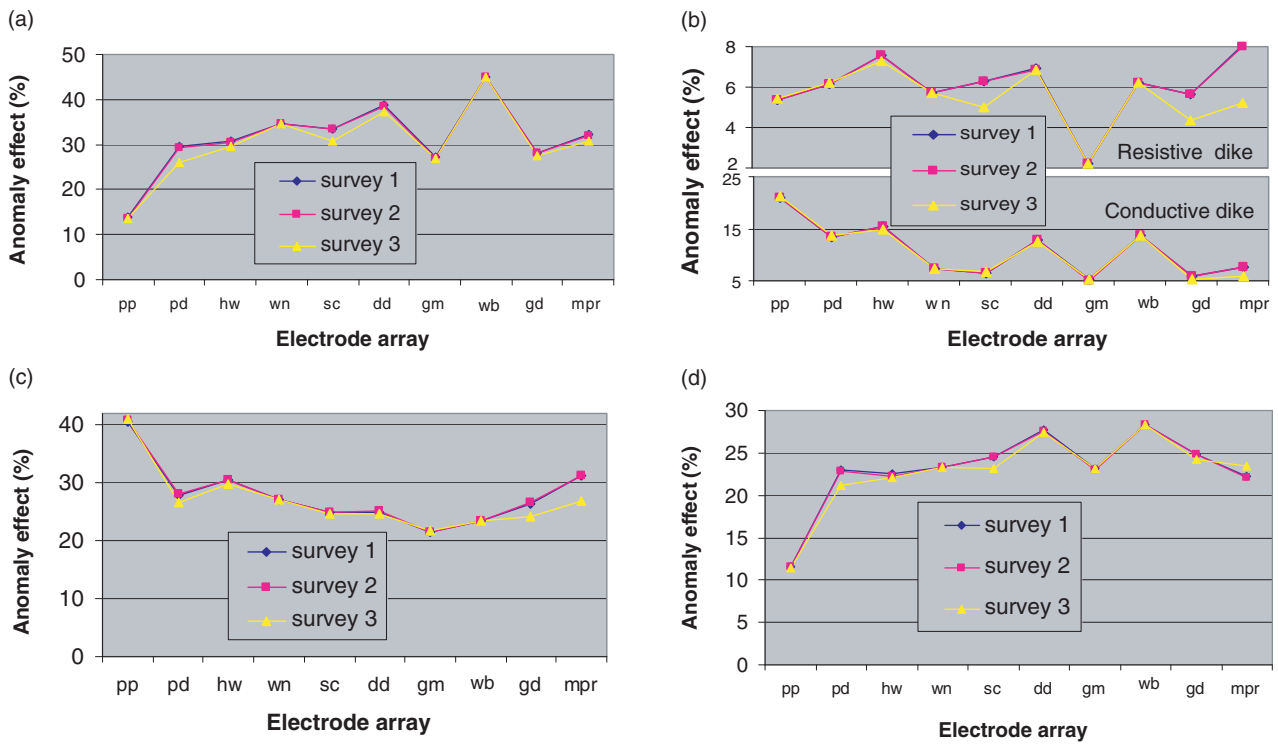

Figure 4 Average absolute anomaly effects of imaging surveys on the four geological models shown in Fig. 3. It can be seen that the anomaly effect of an electrode array varies with the geological model. The three surveying schemes in Table 1 have nearly the same anomaly effects.

Using the anomaly effects (Fig. 4) and the possible noise contamination (Fig. 5), we estimated the signal-to-noise ratios of the imaging surveys for these electrode configurations and synthetic geological models. Figure 7 compares the signal-to-noise ratios of the electrode arrays. From this figure, we can see that, except for the case of the narrow conductive dike, GM and WN have relatively high signal-to-noise ratios, PD and DD give relatively low signal-to-noise ratios, and PP gives high values for the narrow dike and buried dipping blocks and low values for the buried channel and waste ponds models. However, in practice PP would probably give a lower signal-to-noise ratio due to noise picked up by the potential reference electrode.

We should mention that these electrode arrays have differing effects due to spacing errors or small 3D geological disturbances on 2D imaging surveying data. These effects were not included in the synthetic noise applied here. Using analytic analysis and numerical simulations (Zhou and Dahlin 2003), it was shown that the magnitude and the spreading patterns of the spacing errors or the small 3D disturbances differ considerably for the different electrode configurations. For example, 10% in-line spacing errors may have an effect of over 20% on the values for DD, WB and GM data, whereas the other electrode arrays give smaller errors. The different electrode arrays have different spreading patterns of the error effect, which radiate from erroneous electrodes or small 3D disturbances, with the magnitude of the error decreasing with increasing electrode spacing. Artefacts or distortions, close to the erroneous electrodes or the disturbances, appear in the inverted models due to the in-line spacing errors or small 3D geological variations, especially with DD, WB and GM surveys.

IMAGING EXPERIMENTS

The 'observed data' were obtained by adding the potential-dependent random noise (Fig. 5) to the theoretical responses of the synthetic geological models shown in Fig. 3. Three noise levels (average $\leq$10%, $\leq$20%, $\leq$30%) were simulated for each model and survey scheme in Table 1. The commercial software RES2DINV, which offers two inversion options – robust inversion (Loke, Acworth and Dahlin 2003) and smoothness-constrained least-squares inversion (Loke and Dahlin 2002) – individually inverted the 'noise-contaminated' data sets. In principle, the robust inversion is superior to the

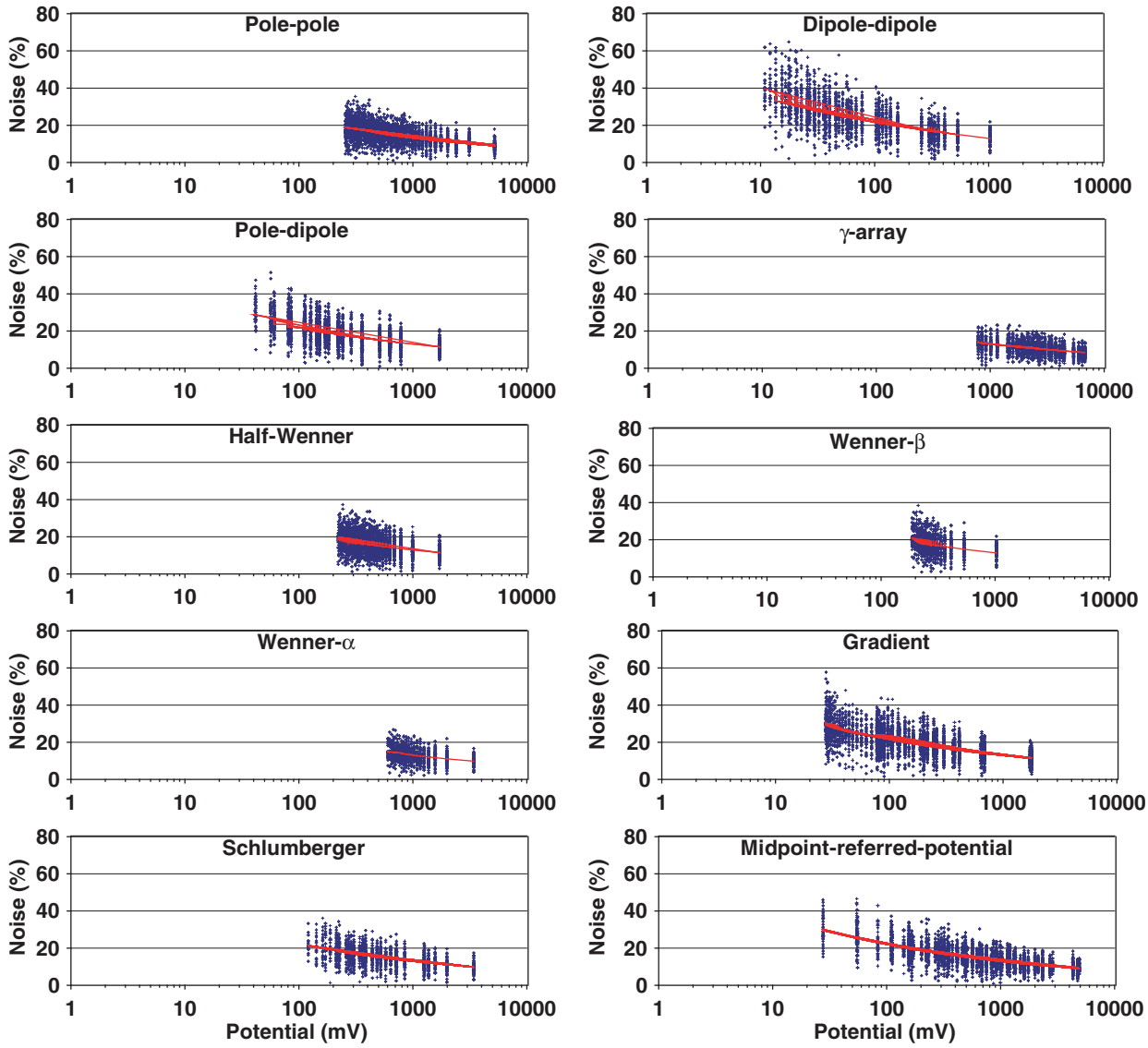

Figure 5 Simulations of the potential noise for 2D resistivity imaging surveys over the conductive narrow dike model (Fig. 2b). The potential noise was generated by the regression function: $Noise = U(1 + R)\beta/100$, which was obtained from the statistical analysis of real data sets (Zhou and Dahlin 2003). U is the potential reading, R is a random number and $\beta = (c_1/U)^{c_2}$. Here we used $c_1 = 8.742 \times 10^7$ and $c_2 = 0.225$.

smoothness-constrained least-squares inversion, because the former attempts to find a model that minimizes the absolute values of the data misfit (L_1-norm) and the latter seeks a smooth model that minimizes the squares of data misfit (L_2-norm). The L_2-norm inversion tends to give greater importance to data points with a larger misfit and this makes it more sensitive to the outliers in the data.

We applied the two inversions to investigate the behaviour of resolution, data density and sensitivity to noise level. From the inversion tests, it was found that the two schemes gave the best results with the initial and minimum damping factors set at 0.15 and 0.03, respectively, with the increase in damping factor with depth set at 1.1 and with iterative recalculation of the Jacobian matrix. Hence, we applied these inversion parameters to all the following experiments. In most of the imaging experiments with noise-free data and noise-contaminated data, the robust inversion gave much better images than the L_2-norm inversions. It was less sensitive to the noise levels and produced fewer artefacts in the inverted models, which is consistent with our real-data experiments (Zhou and Dahlin

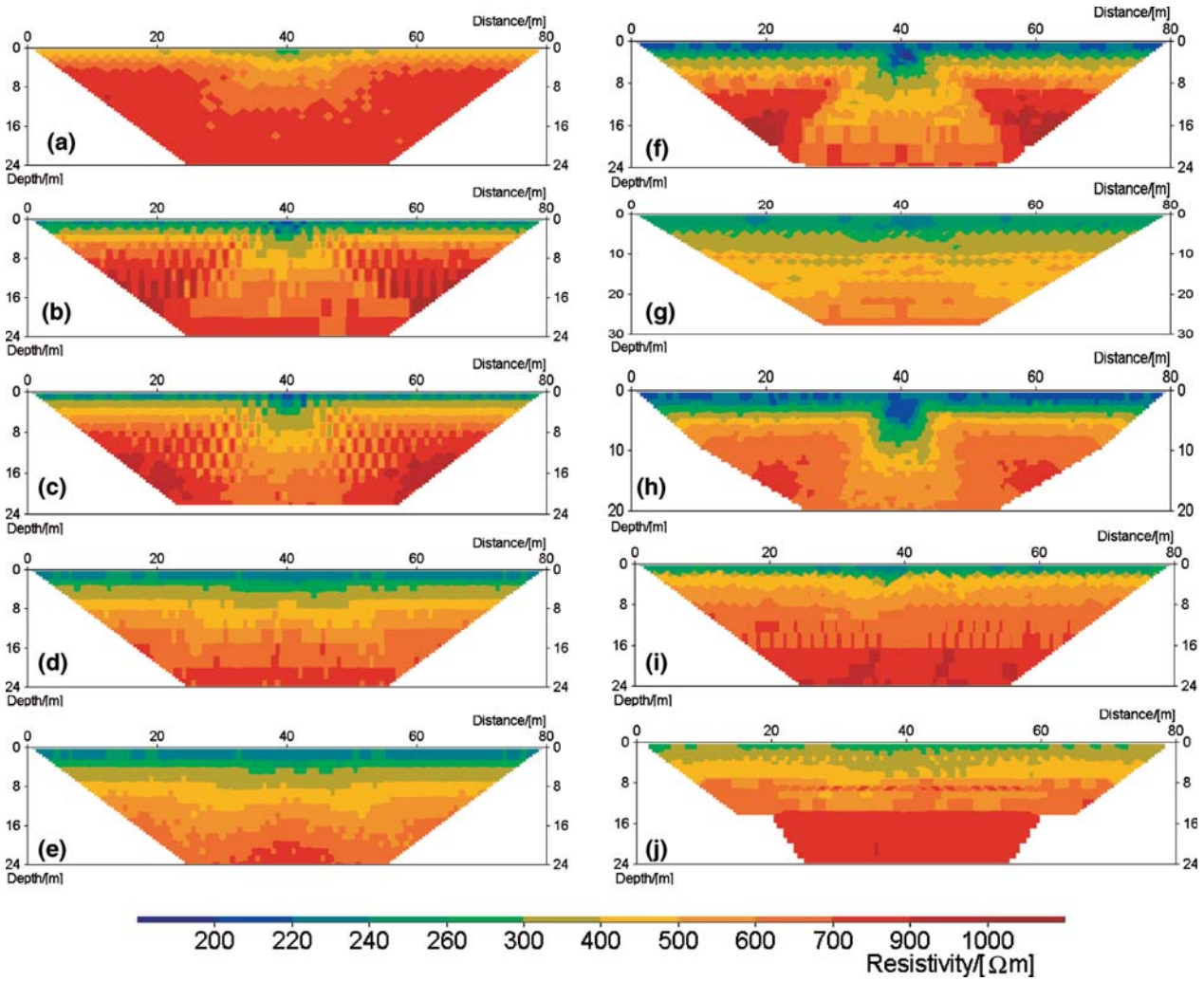

Figure 6 Pseudosections of noise-contaminated apparent resistivity generated with the conductive dike model (see Fig. 3c): (a) pole-pole (PP), (b) pole-dipole (PD), (c) half-Wenner (HW), (d) Wenner-α (WN), (e) Schlumberger (SC), (f) dipole-dipole (DD), (g) γ-array (GM), (h) Wenner-β (WB), (i) multiple gradient array (GD), (j) midpoint-potential-referred measurement (MPR).

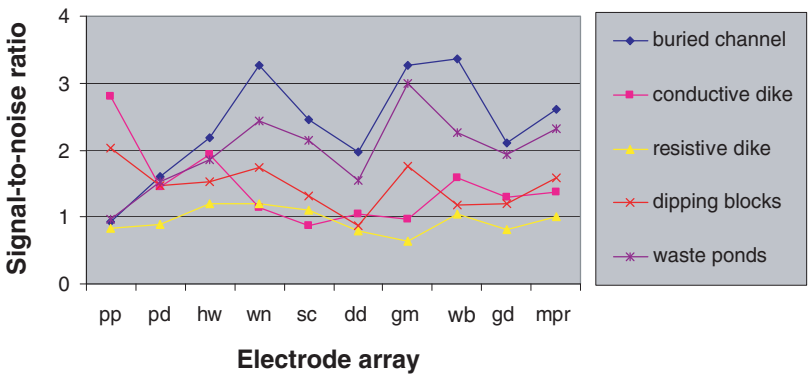

Figure 7 Synthetic signal-to-noise ratios of the imaging surveys obtained with different electrode arrays over the four geological models (see Fig. 3).

2003). The following paragraphs give some views of the synthetic imaging results.

Buried channel

Figure 8 shows the inverted models for the buried channel model (Fig. 3a), obtained with the robust inversion technique using the data of Survey 3 in Table 1, which were contaminated by potential-dependent random noise ranging from a mean of 8.3% for the GM survey to 19.4% for the DD array. From these results, it can be seen that in spite of the relatively low noise levels in these surveys, GM and WB give poor resolution for the bottom of the buried channel (Figs 8g,h). The PD, GD and HW arrays, although they have relatively high noise levels, produced better resolution of the images than the other arrays (Figs 8b,c,i, in which the trapezoidal-shaped channel

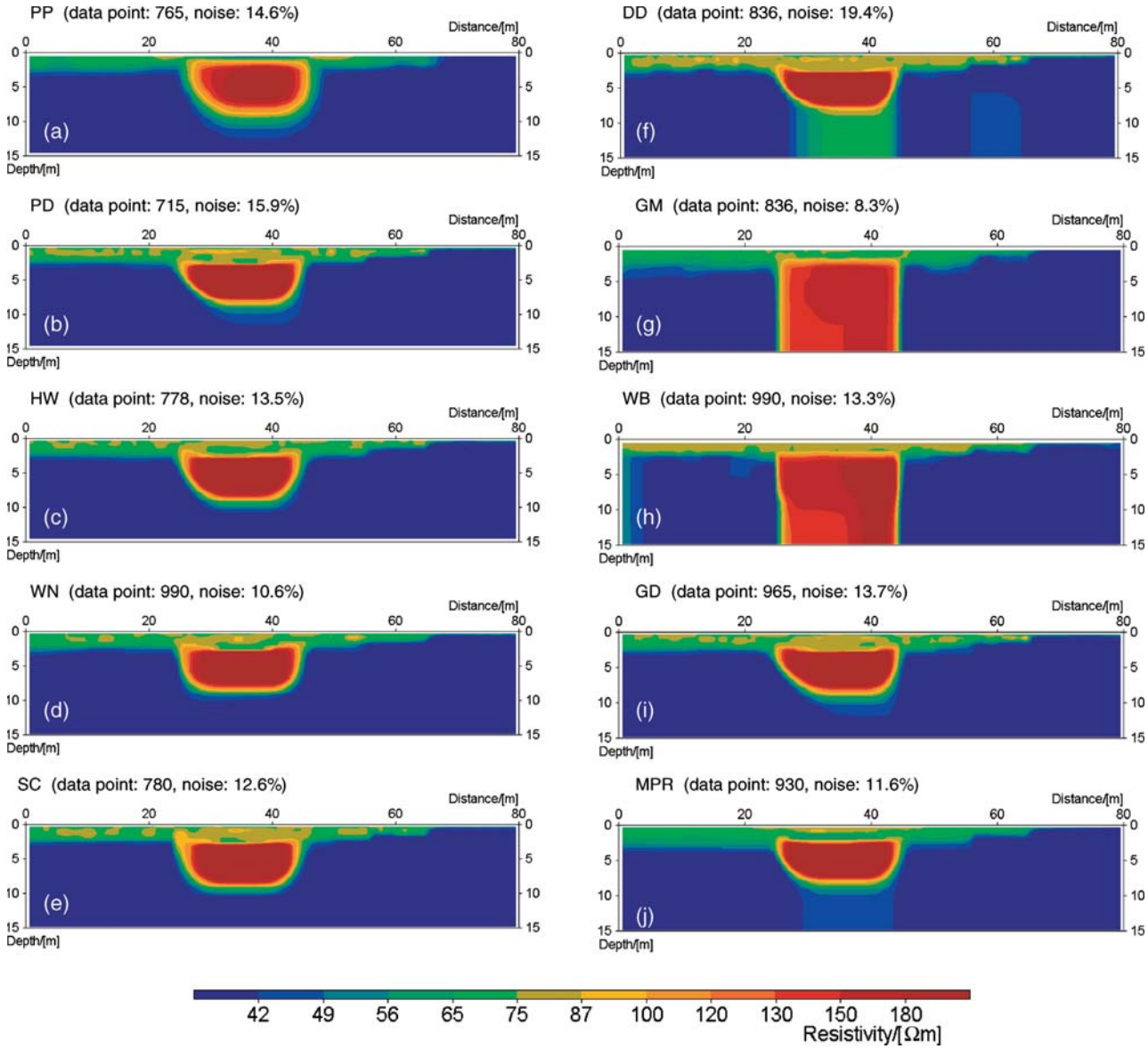

Figure 8 Inverted models using robust inversion for the buried channel shown in Fig. 3(a). Here the data points (Survey 3 in Table 1) and the mean values of the potential-dependent random noise are given for the 10 electrode arrays: (a) PP, (b) PD, (c) HW, (d) WN, (e) SC, (f) DD, (g) GM, (h) WB, (i) GD, (j) MPR.

can be clearly seen). DD also yielded good resolution for this model, but a shadow zone of high resistivity appeared below the target (Fig. 8f), which shows that the deep resolution is not as good as with the PD, HW or GD arrays. This may be partly due to the DD array having the highest noise level (19.4%) of all the arrays, but it is also a consequence of the character of the sensitivity function. It can be seen that SC and MPR produced slightly better resolution of the buried channel than WN (Figs 8d,e,j), but neither of them mapped the trapezoidal shape of the target as well as PD, HW, GD and DD. This indicates that the resolutions of WN and SC, even with relatively low noise contamination (10.6% and 12.6%) and a high signal-to-noise ratio (Fig. 7), do not resolve the shape as well as the PD, HW, GD and DD arrays. This figure also shows that the PP array (Fig. 8a) yielded a reasonably good image, but it apparently did not perform as well as PD, HW, GD and SC. The resolution of PP appears inferior to that of PD, HW, DD, GD, MPR and SC, and it is notable that the thickness of the top layer is poorly mapped.

Narrow conductive dike

Figure 9 shows the robust inversion results from the data of Survey 3 in Table 1 for the narrow conductive dike shown in Fig. 3(b). Here the noise levels were double that of the noise shown in Fig. 5. From these inverted models, it can be seen that DD and GD give the highest resolution and best image for the narrow dike even though the mean value of the potential-dependent random noise reaches 24% and 17%, respectively (Figs 9f,i). The next best results are obtained from PD, HW and MPR, which also give very clear images of the dike (Figs 9b,c,j). GM also performs well for this simple model (Fig. 9g). WN and SC produce a clear image of the dike, but despite having lower random noise than DD, PD, GD and HW, both have distortions on each side of the dike (Figs 9d,e). This must be related to the low anomaly effects (see Fig. 4) and the low signal-to-noise ratios of the two surveys over this model. It implies that these two electrode configurations have very similar imaging behaviour, which is dependent on their electric field distributions and hence the sensitivity functions for this model. PP, which has the best anomaly and signal-to-noise ratio of all these arrays (Figs 4b and 7), gives the worst resolution of the image (Fig. 9a). WB, as a specific case ($n = 1$) of DD, exhibits a decrease in the resolution with depth (Fig. 9h).

Narrow resistive dike

In order to investigate the behaviour of the arrays when imaging a resistive dike, the geometry of the previous model was kept but the resistivities of the dike and host rock were changed to 300 Ωm and 50 Ωm, respectively. Figure 10 shows the results and it can be seen that GM fails to give a correct image of the narrow resistive dike due to the lowest anomaly effect (2.2%) and signal-to-noise ratio (0.6%). In this survey (see Fig. 7), WN and SC yield better images than in the conductive dike case (no distortions on the sides of the dike, as shown in Figs 9d,e), DD, GD and PD still give high resolution of the dike, and PP performs poorly as for the conductive dike. The complementary experiments indicate the following: imaging with GM is unsuitable for the narrow dike; WN and SC may have different imaging qualities for the conductive and resistive dike cases; DD, GD and PD consistently demonstrate powerful imaging abilities for the dike models; SC and MPR give very similar resolution images.

Dipping blocks of sedimentary rock

Figure 11 shows the inverted models of the L_2-norm inversion for the dipping blocks shown in Fig. 3(c). The robust inversion gave images that are too 'blocky' to show the dipping structure when used for the data of Survey 3 in Table 1 (not shown here). Figure 11 shows that DD and PD give much better resolution of the structure than the other arrays although some small artefacts can be seen in the shallow depth. Undoubtedly, these artefacts were caused by the relatively high noise contamination (28% and 22%, respectively) in these two arrays. Meanwhile, it can be seen that WN and PP which have lower noise levels (15% and 20%, respectively) give fewer artefacts than DD and PD, but their images do not clearly indicate the dipping feature (Figs 11a,d). GD and MPR produce better resolution at depth than WN, GM and WB, but not good as that of PD and DD. However, GD achieves the same resolution as these arrays for the higher data densities. If the measurements are made with a multichannel instrument, this data density could be conveniently attained. SC gives a better image than WN (Fig. 11e), but appears to have less resolution near the edges than PD, DD and GD. GM and WB give poor resolution for this model even if the noise levels are not so high as for DD and PD (Figs 11g,h). The two images mostly show a 'vertical blocked structure' instead of a dipping blocked model. It again suggests that although GM and WB coherently exhibit relatively high signal-to-noise ratios (Fig. 7), they cannot compete with the resolution of imaging of the other arrays. Also, these images exhibit a similar behaviour of limited 'penetration depth'. The penetration depth of an array was taken as the maximum depth of the sensitive area of the data and

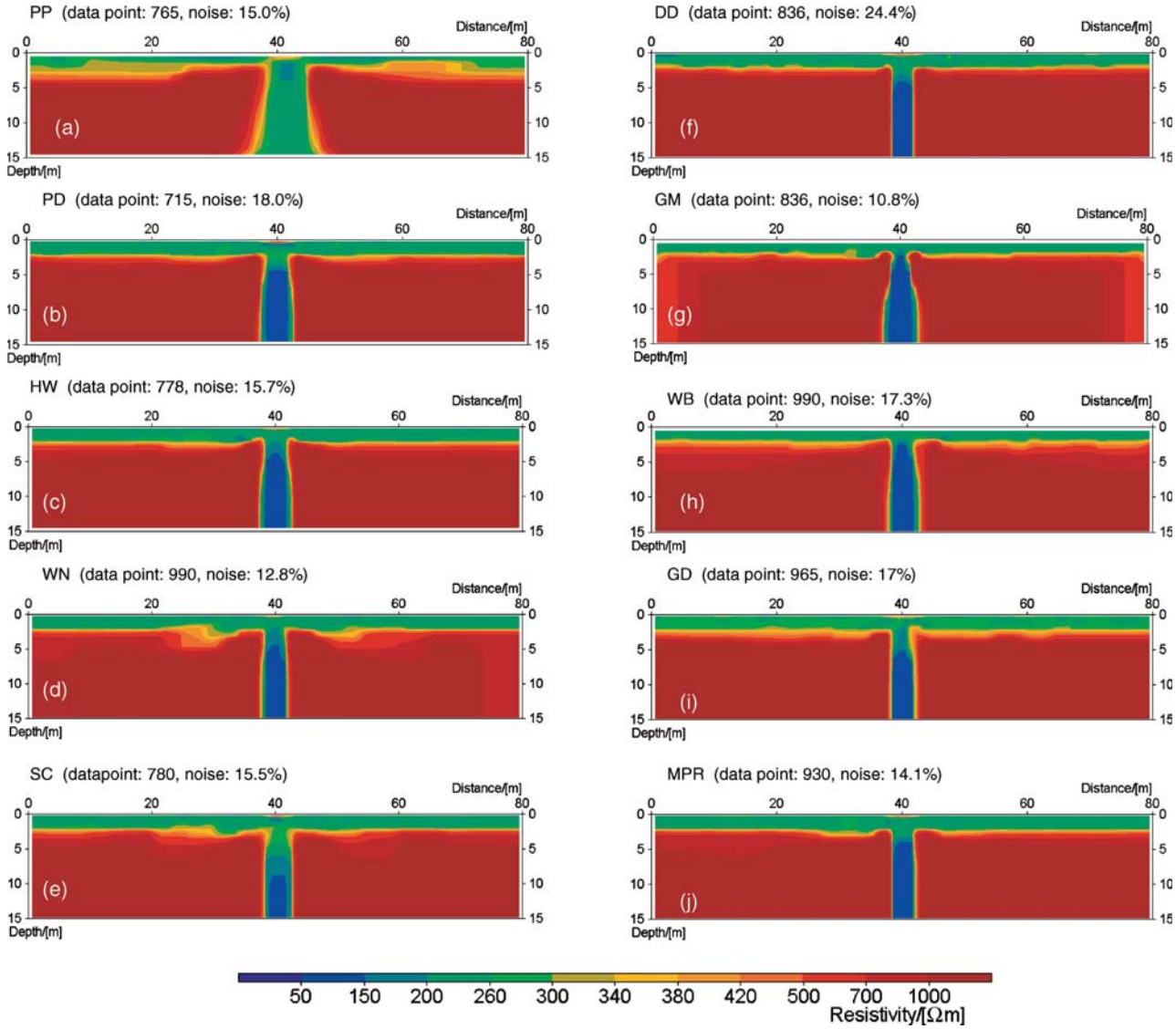

Figure 9 Inverted models using robust inversion for the narrow conductive dike shown in Fig. 3(b). Here the data points (Survey 3 in Table 1) and the mean values of the potential-dependent random noise are given for the 10 electrode arrays: (a) PP, (b) PD, (c) HW, (d) WN, (e) SC, (f) DD, (g) GM, (h) WB, (i) GD, (j) MPR.

beyond the penetration depth, the data lose the capability to resolve the structure.

Oldenburg and Li (1999) suggested two methods to assess the penetration depth of an array. Both methods are based on using different starting models in the inversion procedure to calculate the sensitivity of different areas in the inverted model for a specific data set. Unfortunately, the commercial software RES2DINV that we used here always starts with a homogeneous model, and does not have an option which allows the use of a different initial model. However, by comparing these inverted results with the original model (Fig. 3c) it is easy to distinguish between the well-reconstructed and the poorly resolved parts of the model for the different data sets. These two parts may indicate the sensitive area and the poor-resolution area of the data, respectively, and the boundary between the two areas may be considered as the penetration depth of measurements. These results show that the left lower parts were not well reconstructed. These lost parts or poor-resolution

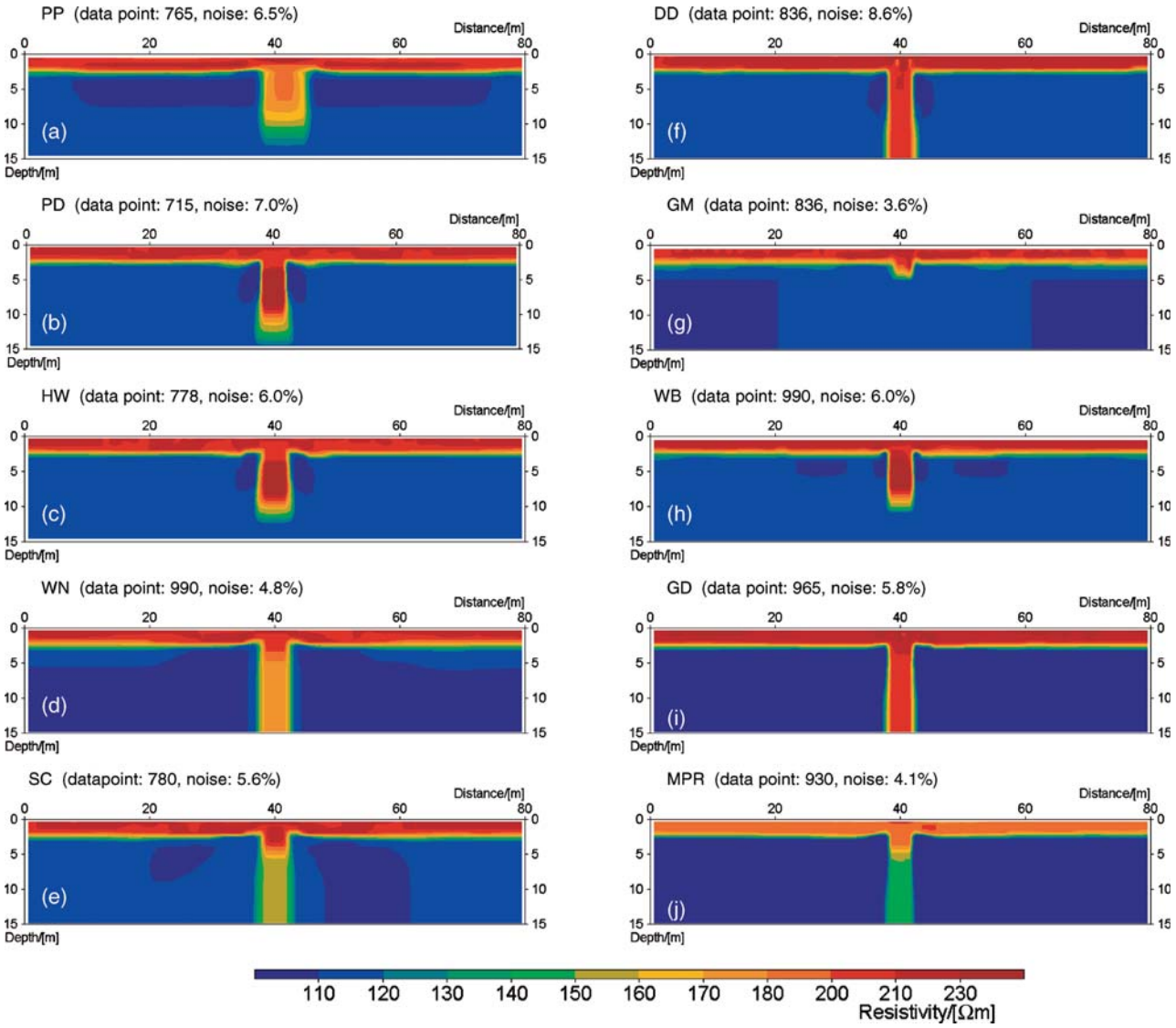

Figure 10 Inverted models using robust inversion for the narrow resistive dike shown in Fig. 3(b). The data points (Survey 3 in Table 1) and the mean values of the potential-dependent random noise are given for the 10 electrode arrays: (a) PP, (b) PD, (c) HW, (d) WN, (e) SC, (f) DD, (g) GM, (h) WB, (i) GD, (j) MPR.

zones are similar for the different arrays. On the right side of the model all the inversions give much better images than on the left side, because the widths of the dipping blocks decrease from right to left. Such structure and poor data coverage at the edge (edge effects) naturally makes it more difficult to image the dipping blocks on the left side from these imaging surveys. The similar trend in all these inverted models implies that the penetration depths of these arrays are not significantly different, apart from the deviation from true dip, because the same maximum separation of electrodes (60 m) was employed for all the arrays.

Waste ponds

Figure 12 shows the inverted models of the waste ponds (Fig. 3d) obtained from the robust inversions. Survey 3 listed in Table 1 was also employed in the imaging surveys. The L_2-norm inversions yielded many more artefacts from the

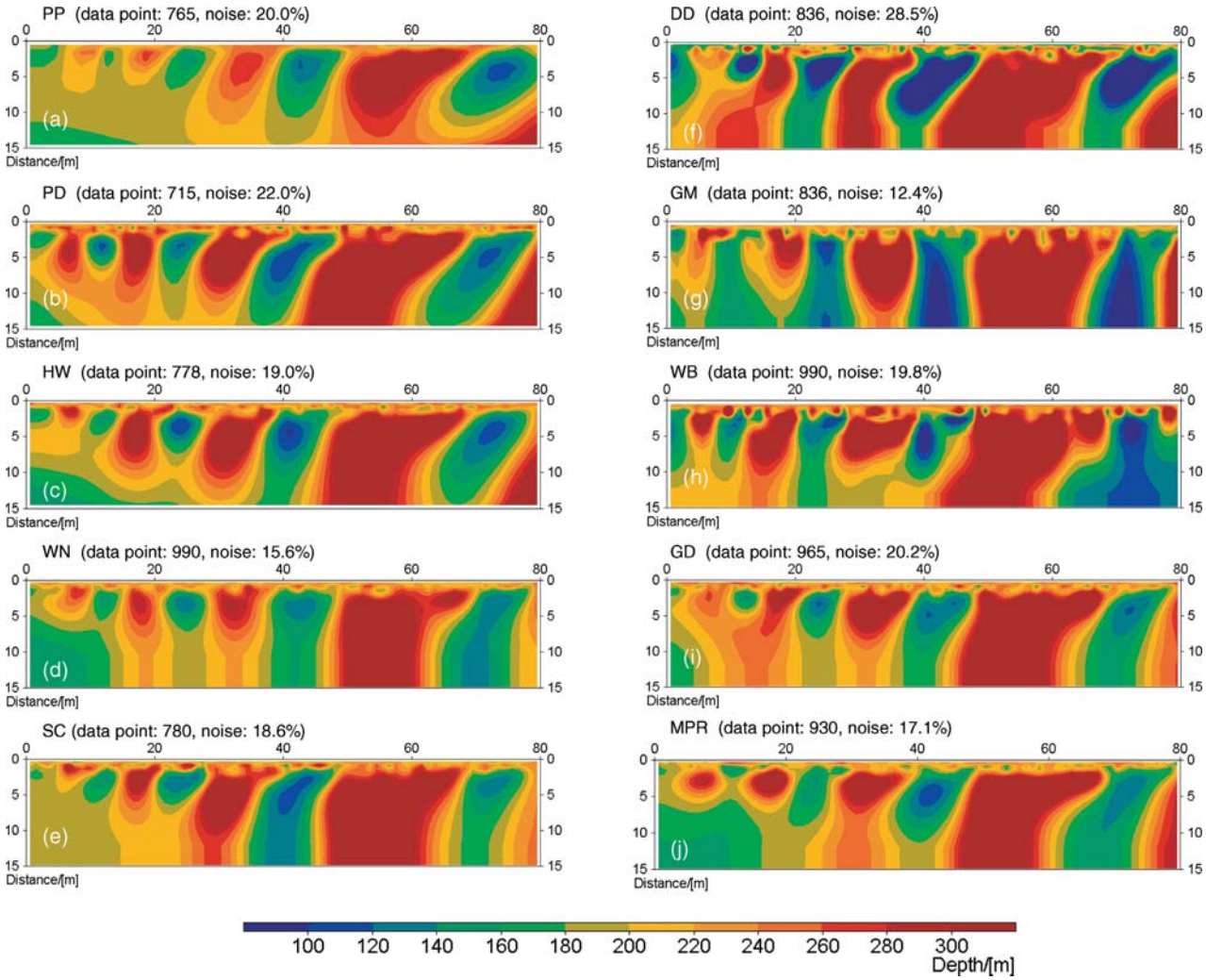

Figure 11 Inverted models using the L_2-norm inversion for the dipping blocks shown in Fig. 3(c). Here the data points (Survey 3 in Table 1) and the mean values of the potential-dependent random noise are given for the 10 electrode arrays: (a) PP, (b) PD, (c) HW, (d) WN, (e) SC, (f) DD, (g) GM, (h) WB, (i) GD, (j) MPR.

noisy data than the robust inversion, especially using the DD, GM and WB arrays. From this figure, it can be seen that all the arrays were able to reconstruct visually six of the nine pits (Fig. 3d), starting from the shallower pits, but they demonstrate varying spatial resolution for these bodies. Obviously, PD, DD, GD and WB produced four of the best images, followed by MPR, SC, WN and HW, and then GM and PP. Meanwhile, their common missing features or poorly reconstructed zones can be recognized in the images. These arrays all fail to give clear images for the last three deep pits. Once again, this shows that, with the same maximum separation in imaging surveys, all electrode configurations give similar penetration depths in the inverted model.

To investigate the change in the penetration depth with resistivity contrast, we reduced the resistivity contrast by increasing the resistivities of the nine pits from 10 Ωm to 50 Ωm and repeated these experiments. Similar images to Fig. 12 were obtained, except that one deeper pit was lost. This means that the penetration depth of an array depends mainly on the resistivity contrast and maximum separation of the electrode array employed in the imaging survey, and also on the size of the target relative to the depth of burial. However, it should also

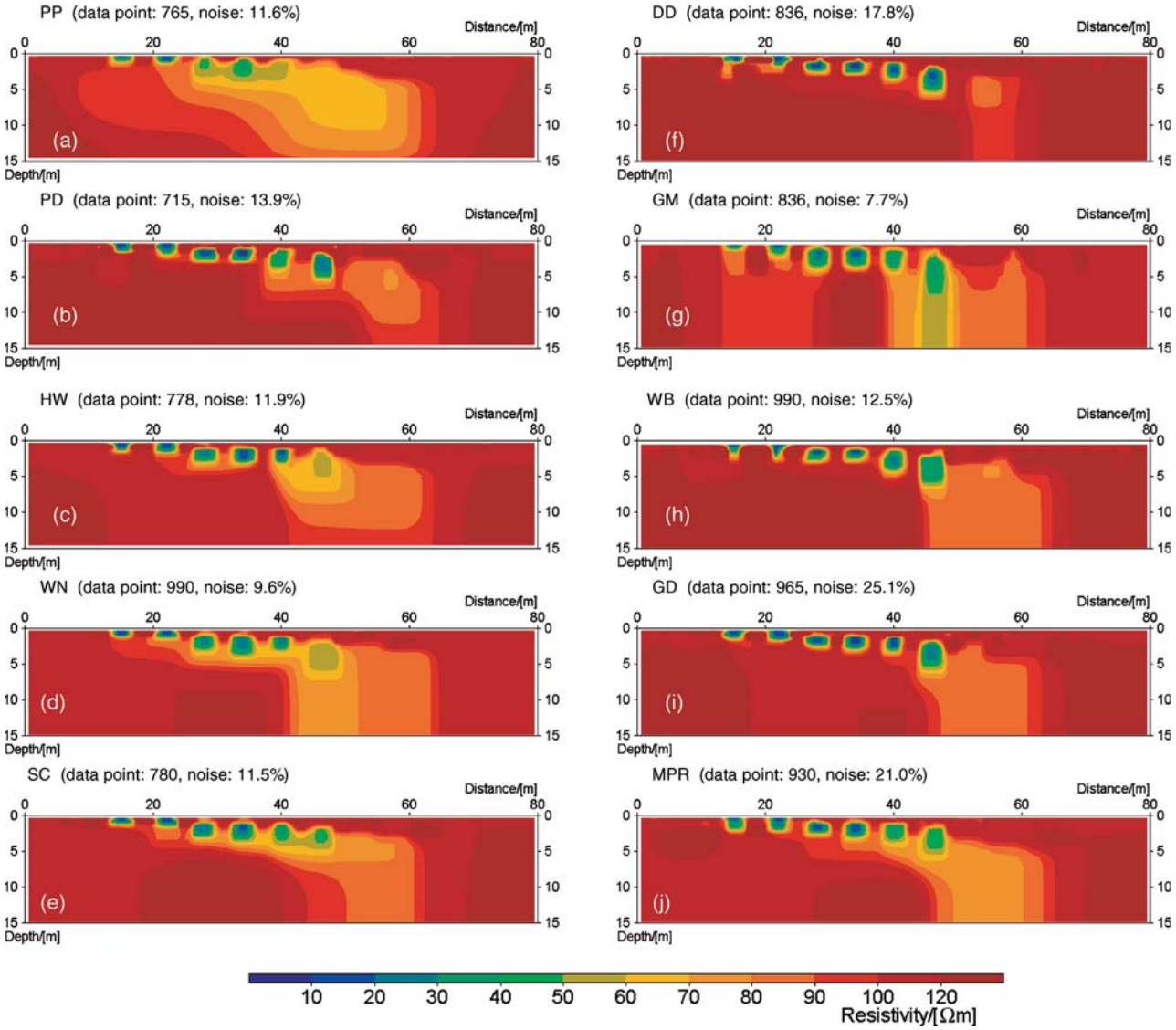

Figure 12 Inverted models using the robust inversion for the waste ponds shown in Fig. 3(d). Here the data points (Survey 3 in Table 1) and the mean values of the potential-dependent random noise are given for the 10 electrode arrays: (a) PP, (b) PD, (c) HW, (d) WN, (e) SC, (f) DD, (g) GM, (h) WB, (i) GD, (j) MPR.

be noted that the resolution of the deepest anomalous bodies may be affected by edge effects, due to the reduced data cover for long electrode separation near the end of the electrode layout.

Data density

As mentioned above, there are many choices of imaging surveying schemes for PP, PD, HW, SC, DD, GM, GD and MPR arrays, using the same 81-electrode layout and the same maximum separation of electrodes. Table 1 gives some examples that define different numbers of data points or data density. In general, a dense distribution of data points helps to improve the spatial resolution of imaging, especially for small targets of a similar size to the basic spacing. Dahlin and Loke (1998) gave an example of the resolution change with data density for a WN imaging survey. They proved that it is necessary to employ either a small spacing or dense data in a WN imaging survey to obtain high resolution of the narrow dike. However, it should be pointed out that these results were based on

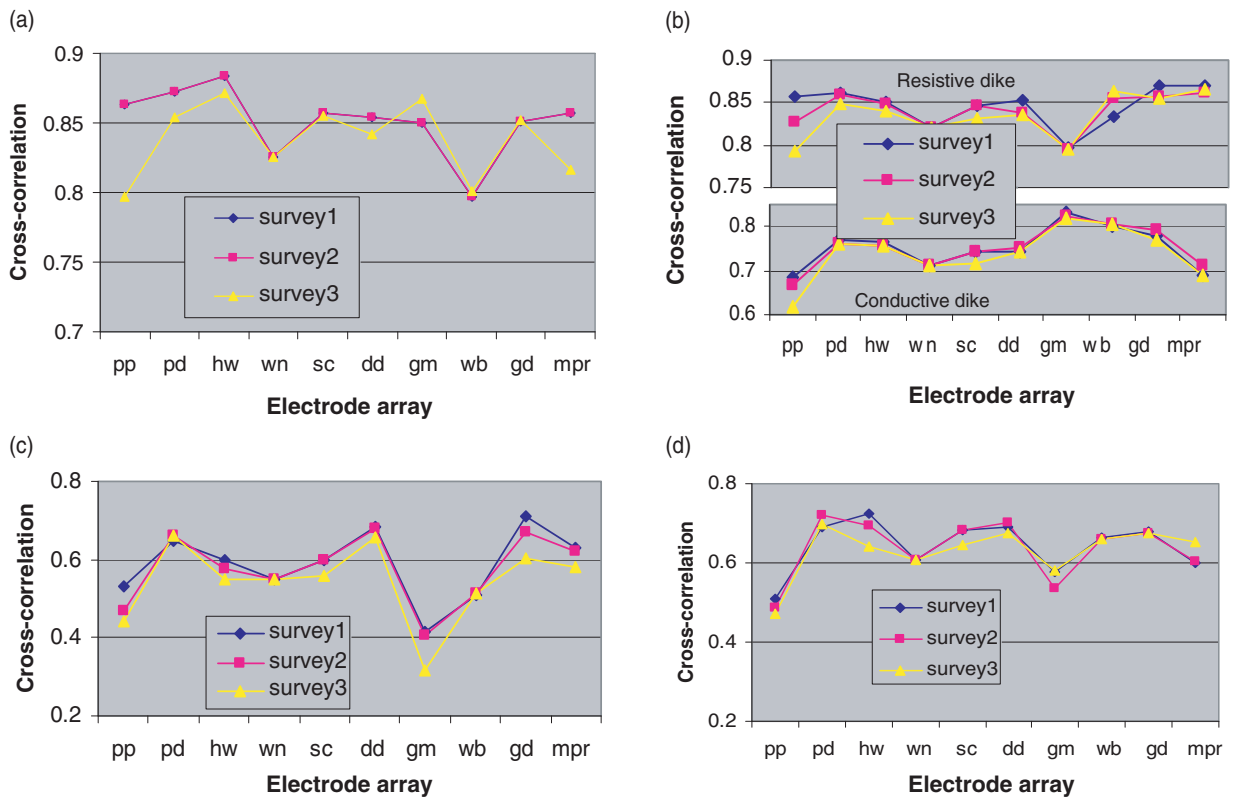

Figure 13 Cross-correlation curves of the L_1-norm inverted models with the true models given in Fig. 3. (a) Buried channel; (b) narrow dike; (c) dipping blocks; (d) waste ponds. The three surveying schemes are given in Table 1.

experiments with lower data densities than in this work. Here, in order to detect the variation in imaging quality with the data density of an electrode layout, as well as to investigate an efficient surveying scheme of the arrays for a given electrode layout, we repeated all previous imaging experiments with the two other surveying schemes with different data densities: Survey 1 and Survey 2 in Table 1. We then calculated the cross-correlation values of the inverted models with the true models. The cross-correlation value represents quantitatively the match of two images, which may reflect the quality of the imaging results. Figure 13 shows the cross-correlation curves of the three surveying schemes against the different electrode arrays for the L_1-norm inversion results, and the corresponding L_2-norm inversion results are shown in Fig. 14.

Figures 13 and 14 summarize the imaging quality of the arrays for the five models, as well as illustrating the variation in the imaging quality for the three surveying schemes. It shows that the three surveying schemes, although having quite different data densities, generally gave similar results with limited changes in the imaging quality of the arrays. This means that, with the same electrode layout and maximum separation of electrodes, the imaging quality of an array survey is not very sensitive to the data density within the limits tested here. However, an increase from the lowest to the intermediate data density gives significant detail resolution enhancement in some cases. In other words, the high data densities, greater than those that can be achieved with WN and WB with an electrode layout, in most cases did not significantly improve the imaging quality, even though it takes much more time to acquire high-density data in a field with a single-channel multi-electrode data acquisition system. An exception is PP, which benefits significantly from more data points for a couple of the models. However, it may be possible that the resolution limitation for the other arrays lies partly in the cell division of the inversion model, and that inversion with a finer cell division than that used here, in combination with the highest data density, could result in better definition of the models.

These experiments imply that an efficient imaging survey may be employed by choosing appropriate parameters n and a for the arrays. For example, Survey 3 in Table 1 for PD, HW, DD GD, MPR and SC arrays, which did not necessarily

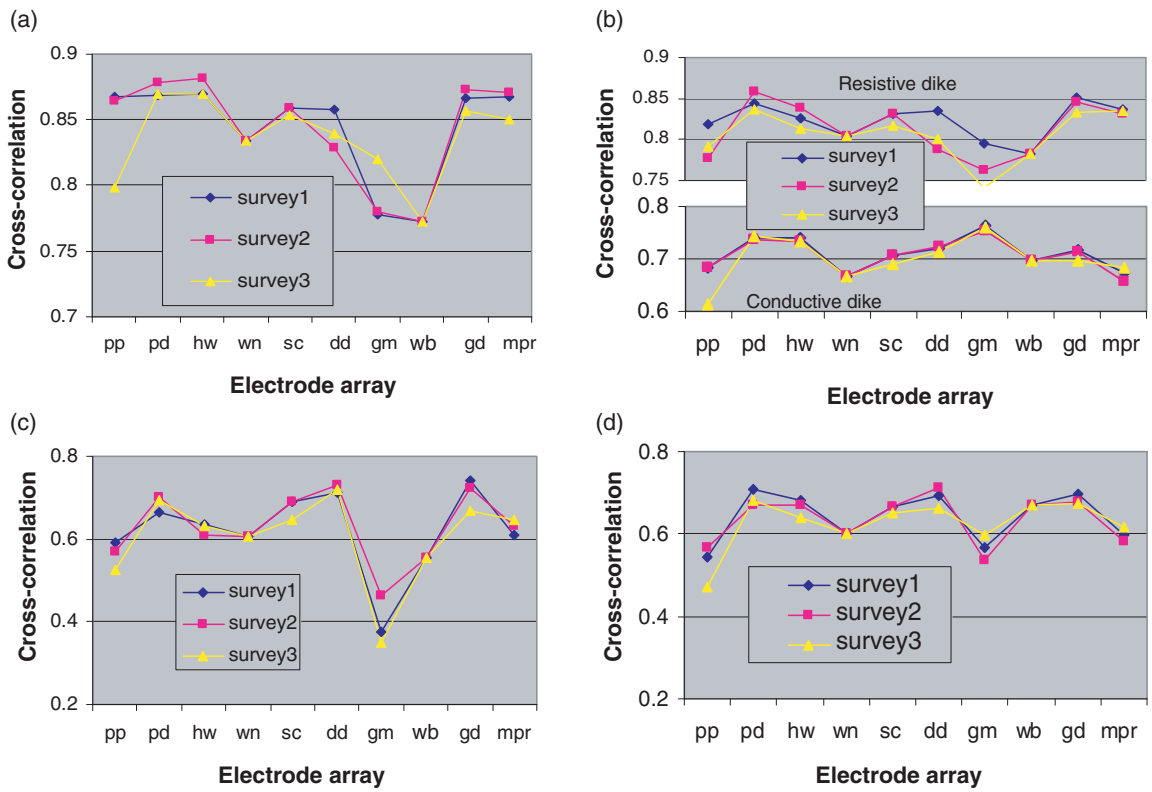

Figure 14 Cross-correlation curves of the L_2-norm inverted models with the true models given in Fig. 3. (a) Buried channel; (b) narrow dike; (c) dipping blocks; (d) waste ponds. The three surveying schemes are given in Table 1.

scan all n and a in the imaging surveys, yielded resolutions of the images comparable to those of the higher density data sets.

Comparing Fig. 14 with Fig. 13, it can be seen that the behaviour of the cross-correlation curves of the L_2-norm inversion is generally similar to that of the L_1-norm inversion for the five models. The curves show that except for the dipping block model, the L_1-norm inversion gives slightly larger cross-correlation values than the L_2-norm inversion. In fact, on inspection we found that even when the cross-correlation values of the inversions are close, the results from the L_1-norm inversion have fewer artefacts.

The imaging quality of some mixed-array surveys, such as WN + PD, WN + HW, WN + DD and WN + WB, has also been examined. The results (not given here) show that the image from each of the mixed arrays is similar to the better resolved individual image, i.e. the inverted results from WN + PD, WN + HW, WN + DD and WN + WB surveys are similar to those obtained from PD, HW, DD and WB. PD, HW and DD may provide higher image resolution than WN, but a mixed survey with data from a lower resolution array, such as WN, gives little or no improvement in imaging quality.

SUMMARY AND CONCLUSIONS

From our numerical simulations, we may summarize the main advantages and disadvantages of these arrays for 2D resistivity imaging.

PP

This simple electrode configuration makes it easy to automate the data acquisition and to check data quality with reciprocity in the field, but it employs two remote electrodes that limit its application to accessible sites. The anomaly effect and signal-to-noise ratio of the imaging survey may be relatively high or low, depending on the geological model, but the theoretical noise contamination generally remains at moderate levels compared with other arrays. However, the imaging resolution ranks low among the 10 electrode configurations. In addition,

ambient (telluric) noise may be picked up by the remote potential electrode. This was not included in the modelling above.

PD and HW

Although having moderate anomaly effects and relatively low signal-to-noise ratios, both can yield better spatial resolution images than PP, SC and WN. At some loss of spatial resolution, a somewhat better signal-to-noise ratio may be obtained with HW. This is due to the strengthened measured signals obtained from the increased potential electrode spacing and it effectively reduces the noise contamination. One disadvantage is that the use of one remote electrode limits the surveys to accessible sites. Another is that the remote electrode complicates data quality checks via reciprocal measurements, since the noise at the remote potential electrode will be higher.

WN and SC

These two arrays have similar imaging ability due to the resemblance of their electric field and measurements. Their main strength is in their good depth determination relative to the other arrays. As a special case of SC, WN generally has less noise contamination and better signal-to-noise ratios than SC, and also than PD, HW, DD and WB arrays (except in the case of the narrow dike). However, the spatial resolution of WN is poorer than that of the PD, DD, HW and SC arrays, while the SC array, even with a slight reduction in the signal-to-noise ratio, may offer better imaging resolution. The WN and SC reciprocal configuration surveys both tend to pick up more noise than the normal configuration when assessing the data quality using reciprocal measurements. This is also a limiting factor for SC in multichannel applications, since a reciprocal array would be necessary to make use of the many measurement channels.

DD and WB

In general, DD has relatively high anomaly effects but is more at risk of noise contamination than other arrays, so it often produces lower signal-to-noise ratios in surveys, compared with WB, WN and GM. DD and WB both have symmetric electrode configurations for normal and reciprocal measurements. This facilitates the data quality control needed to obtain reliable well-resolved images. The imaging resolution of DD is comparable to PD and better than the other arrays, particularly for the location of vertical and dipping structures, whereas the depth resolution is not the best. WB, a special case of DD, has a higher signal-to-noise ratio than the DD array, but it has, in some cases, much lower spatial resolution than DD. These two arrays are much more sensitive to spacing errors (Zhou and Dahlin 2003) and the presence of 3D geological bodies than other arrays (Dahlin and Loke 1997). The highest factor n used in the modelling was 6, and it is often not advisable to go beyond that value in real situations, due to the resulting very low signal-to-noise ratios.

GM

The main advantage of this array is that the noise contamination of its imaging survey is the lowest of all the arrays, but its anomaly effects and signal-to-noise ratios are not consistently high, and its spatial resolution is not as good as other arrays.

GD and MPR

Both configurations are suitable for multichannel data acquisition. The numerical experiments show that GD scanning measurements can produce an image to compete with those of PD, DD and SC. It gives well-resolved resistivity images. MPR has a higher signal-to-noise ratio than GD but a somewhat lower spatial image resolution. The resolution of MPR is comparable to that of WN when used with a multichannel-recording instrument, which gives more efficient data acquisition.

Accordingly, this work strongly recommends the electrode configurations GD, PD, DD and SC. GD, which is ideal for multichannel-recording configurations, is also a prime choice for single-channel data acquisition systems. MPR may also be an option for multichannel-recording configurations, because of its lower noise sensitivity. However, for several of the models tested, it has a poorer resolution than GD. The final choice for a particular survey depends on the site conditions, field logistics and the target of the survey. The good surveying qualities, namely the relatively high anomaly effect, the high signal-to-noise ratio, and the low noise contamination of the WN, WB and GM arrays, do not always produce the best-resolved images. This is due to the limited resolution capabilities of these arrays.

ACKNOWLEDGEMENTS

The work presented here was supported by research grants from Elforsk, Svenska Kraftnät, DSIG (Dam Safety Interest Group), the Wenner-Gren Foundation, the Swedish

Institute and the Carl Trygger's Foundation, which are gratefully acknowledged. We are indebted to Professor Dale Morgan for sharing his experience of the multiple gradient array.

REFERENCES

Bernstone C. and Dahlin T. 1996. Electromagnetic and DC resistivity mapping of waste deposits and industrial sites – experiences from southern Sweden. 58th EAGE conference, Amsterdam, The Netherlands, Extended Abstracts M014.

Chambers J., Ogilvy R., Meldrum P. and Nissen J. 1999. 3D resistivity imaging of buried oil- and tar-contaminated waste deposits. *European Journal of Environmental and Engineering Geophysics* **4,** 3–15.

Dahlin T. 1993. *On the automation of 2D resistivity surveying for engineering and environmental applications*. PhD thesis, Lund University.

Dahlin T. 1996. 2D resistivity surveying for environmental and engineering applications. *First Break* **14,** 275–283.

Dahlin T. and Loke M.H. 1997. Quasi-3D resistivity imaging: mapping of 3D structures using two dimensional DC resistivity techniques. *Proceedings of the 3rd Environmental and Engineering Geophysics Meeting*, Aarhus, Denmark, Expanded Abstracts, pp. 143–146.

Dahlin T. and Loke M.H. 1998. Resolution of 2D Wenner resistivity imaging as assessed by numerical modeling. *Journal of Applied Geophysics* **38,** 237–249.

Daily W. and Owen E. 1991. Crosshole resistivity tomography. *Geophysics* **56,** 1228–1235.

LaBrecque D., Miletto M., Daily W., Ramirez A. and Owen E. 1996. The effects of 'Occam' inversion of resistivity tomography data. *Geophysics* **61,** 538–548.

Li Y.G. and Oldenburg D.W. 1992. Approximative inverse mapping in DC resistivity problems. *Geophysical Journal International* **109,** 343–362.

Loke M.H., Acworth I. and Dahlin T. 2003. A comparison of smooth and blocky inversion methods in 2-D electrical imaging surveys. *Exploration Geophysics* **34,** 182–187.

Loke M.H. and Barker R.D. 1995. Least-squares deconvolution of apparent resistivity pseudosections. *Geophysics* **60,** 1682–1690.

Loke M.H. and Barker R.D. 1996. Rapid least-squares inversion of apparent resistivity pseudosections by a quasi-Newton method. *Geophysical Prospecting* **44,** 131–152.

Loke M.H. and Dahlin T. 2002. A comparison of the Gauss-Newton and quasi-Newton methods in resistivity imaging inversion. *Journal of Applied Geophysics* **49,** 149–162.

Militer H., Rosler R. and Losch W. 1979. Theoretical and experimental investigations for cavity research with geoelectrical resistivity methods. *Geophysical Prospecting* **27,** 640–652.

Olayinka A. and Yaramanci U. 2000. Assessment of the reliability of 2D inversion of apparent resistivity data. *Geophysical Prospecting* **48,** 293–316.

Oldenburg D.W. and Li Y.G. 1999. Estimating depth of investigation in dc resistivity and IP surveys. *Geophysics* **64,** 403–416.

Park S.K. and Van G.P. 1991. Inversion of pole-pole data for 3-D resistivity structure beneath arrays of electrodes. *Geophysics* **56,** 951–960.

Sasaki Y. 1992. Resolution of resistivity tomography inferred from numerical simulation. *Geophysical Prospecting* **40,** 453–463.

Sasaki Y. 1994. 3-D resistivity inversion using the finite-element method. *Geophysics* **59,** 1839–1848.

Shima H. 1992. 2-D and 3-D resistivity imaging reconstruction using crosshole data. *Geophysics* **55,** 682–694.

Storz H., Storz W. and Jacobs F. 2000. Electrical resistivity tomography to investigate geological structures of the earth's upper crust. *Geophysical Prospecting* **48,** 455–471.

Van G.P., Park S.K. and Hamilton P. 1991. Monitoring leaks from storage ponds using resistivity methods. *Geophysics* **56,** 1267–1270.

Zhou B. and Dahlin T. 2003. Properties and effects of measurement errors on 2D resistivity imaging. *Near Surface Geophysics* **1,** 105–117.

Zhou B. and Greenhalgh S.A. 2000. Crosshole resistivity tomography using different electrode configurations. *Geophysical Prospecting* **48,** 887–912.